A Monte Carlo pencil beam scanning model for proton treatment plan simulation using GATE/GEANT4

View the article online for updates and enhancements.

You may also like

A Monte Carlo pencil beam scanning model for proton treatment plan simulation using GATE/GEANT4

L Grevillot[1,2]**, D Bertrand**[2]**, F Dessy**[2]**, N Freud**[1] **and D Sarrut**[1]

[1] Université de Lyon, CREATIS; CNRS UMR5220; Inserm U1044; INSA-Lyon; Université Lyon 1; Centre Léon Bérard, Lyon, France.
[2] IBA, B-1348, Louvain-la Neuve, Belgium.

E-mail: loic.grevillot@creatis.insa-lyon.fr

Abstract

This work proposes a generic method for modeling scanned ion beam delivery systems, without simulation of the treatment nozzle and based exclusively on beam data library (BDL) measurements required for treatment planning systems (TPS). To this aim, new tools dedicated to treatment plan simulation were implemented in the Gate Monte Carlo platform. The method was applied to a dedicated nozzle from IBA for proton pencil beam scanning delivery. Optical and energy parameters of the system were modeled using a set of proton depth–dose profiles and spot sizes measured at 27 therapeutic energies. For further validation of the beam model, specific 2D and 3D plans were produced and then measured with appropriate dosimetric tools. Dose contributions from secondary particles produced by nuclear interactions were also investigated using field size factor experiments. Pristine Bragg peaks were reproduced with 0.7 mm range and 0.2 mm spot size accuracy. A 32 cm range spread-out Bragg peak with 10 cm modulation was reproduced with 0.8 mm range accuracy and a maximum point-to-point dose difference of less than 2%. A 2D test pattern consisting of a combination of homogeneous and high-gradient dose regions passed a 2%/2 mm gamma index comparison for 97% of the points. In conclusion, the generic modeling method proposed for scanned ion beam delivery systems was applicable to an IBA proton therapy system. The key advantage of the method is that it only requires BDL measurements of the system. The validation tests performed so far demonstrated that the beam model achieves clinical performance, paving the way for further studies toward TPS benchmarking. The method involves new sources that are available in the new Gate release V6.1 and could be further applied to other particle therapy systems delivering protons or other types of ions like carbon.

(Some figures in this article are in colour only in the electronic version)

1. Introduction

The physical advantage of hadron therapy over conventional radiotherapy is better dose conformation to the tumor and a lower integral dose to healthy tissues (Suit *et al* 2010). It has been shown that the integral dose delivered by proton therapy is about half that of intensity modulated radiation therapy (Lomax *et al* 1999). In the case of heavier ions like carbon ions, an additional biological effect is produced in the tumorous area, allowing us to treat radio-resistant tumors (Amaldi and Kraft 2005). Pencil beam scanning (PBS) delivery (also called active scanning) is currently the most advanced technique for ion-beam therapy. It has been used since the end of 1996 at the Paul Scherrer Institute (PSI) in Switzerland for proton therapy (Lomax *et al* 2004) and since 1997 at the Gesellschaft für Schwerionenforschung (GSI) in Germany with carbon-ions (Amaldi and Kraft 2005). The superior ballisitic of dose distributions obtained with ions makes the treatment planning quality assurance process more complex. Monte Carlo codes have been used to benchmark treatment planning systems (TPS) for many years in conventional radiation therapy (Chetty *et al* 2007, Rogers 2006, Verhaegen and Seuntjens 2003). Some dedicated Monte Carlo codes have been developed for conventional radiotherapy (Kawrakow and Walters 2006) and proton therapy (Tourovsky *et al* 2005). Using a generalistic Monte Carlo code, like Geant4, makes it possible to evaluate combined treatment modalities such as, for instance, those using combinations of photon and proton beams (Seco *et al* 2007). Geant4 has been used extensively at the Massachusetts General Hospital in Boston for proton therapy applications using passive spreading techniques (Paganetti *et al* 2008). In this work, we used the Geant4-based Gate toolkit release V6.0 (Jan *et al* 2011) combined with Geant4.9.2p04 for active beam delivery simulations. Initially, Gate was developed to facilitate the use of Geant4 for TEP and SPECT simulations (Jan *et al* 2004). Later, the capabilities of the Gate platform have been extended to other type of medical applications, like radiation therapy (Grevillot *et al* 2011, Jan *et al* 2011). For passive spreading irradiation, it was found necessary to simulate beam interactions throughout the nozzle, because the spreading, modulation and shaping of the beam are fully determined by the different elements encountered in the nozzle (Paganetti *et al* 2004, Cirrone *et al* 2005, Stankovskiy *et al* 2009). In contrast, for active beam delivery, only few elements are present in the nozzle. They do not actively participate in the shaping of the beam, even if they may slightly modify its physical properties. Recently, Monte Carlo models of an active beam scanning proton therapy nozzle have been proposed by the MD Anderson Cancer Center using Geant4 (Peterson *et al* 2009) and MCNPX (Sawakuchi *et al* 2010), by simulating the beam interactions inside the nozzle. The advantage of such a method is the detailed description of the beam interactions within each element of the nozzle that might contribute to the beam spreading and secondary particle production. In contrast, we propose an alternative and generic method allowing us to simulate active beam delivery systems for ion-therapy, without simulating the treatment nozzle. The key advantage of our method is that it only requires the beam data library (BDL) measurements of the system, which are used by TPS manufacturers to create the beam model. This modeling technique relies on the fact that the nozzle elements do not have a strong influence on the beam characteristics. Moreover, their impact will be somehow included in the BDL measurements and therefore indirectly taken into account in the modeling. The proposed method has been tested for an IBA's proton therapy active scanning system, but we believe that it could be applied to other types of ions and delivery systems. The tools presented in this paper have been released in the new Gate version V6.1, which is compatible with Geant4.9.3 and Geant4.9.4 releases.
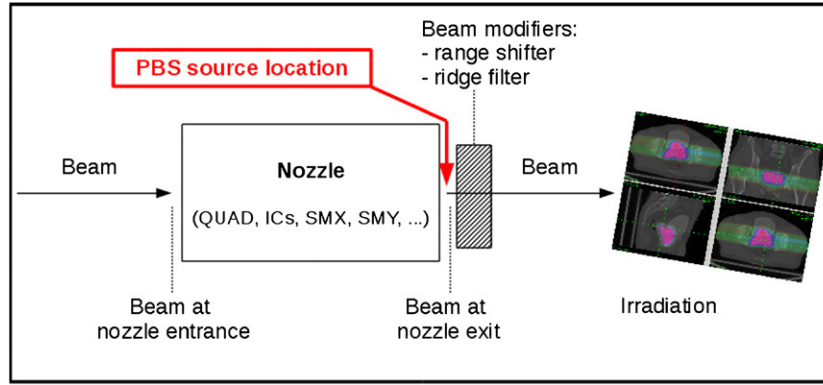
Figure 1. Treatment delivery system from the nozzle entrance. The main components of the nozzle are the quadrupoles (QUAD), the scanning magnets in the x and y directions (SMX, SMY), the ionizations chambers (ICs) and the vacuum windows. When leaving the nozzle, the beam can still encounter beam modifiers before it reaches the patient. The proposed source model starts right at the nozzle exit, allowing us to include such geometries in the simulation.

2. Materials and methods

2.1. Nozzle output beam modeling method

In this section, we describe a generic method to determine the physical properties of the delivery system, based on a set of reference measurements (see section 2.2). BDL measurements characterize the beam at the nozzle exit, before it reaches the patient. In contrast, each single pencil beam of a DICOM RT PLAN is characterized by its energy at the nozzle entrance. A schematic view of the treatment delivery system is presented in figure 1.

Therefore, it appears necessary to characterize the physical properties of the beam at the nozzle exit as a function of the beam energy at the nozzle entrance. To this aim, we have chosen to create a new source in Gate called *GateSourcePencilBeamScanning*, allowing us to define single pencil beams (section 2.1.1). A second source called *GateSourceTPSPencilBeam* was next developed in order to simulate bundles of single pencil beams such as used in clinical practice (section 2.1.2).

2.1.1. GateSourcePencilBeamScanning.
A pencil beam is characterized by its energy and optical properties (figure 2). The energy spectrum is considered Gaussian, with a mean energy E_0 and an energy spread σ_E (standard deviation). Optical properties are independent of energy properties. Optical properties are described by the following three parameters in the x and y directions (+z being the default direction of the beam):

- spatial beam spread distribution (beam or spot size) σ_x in x and σ_y in y
- angular spread distribution (beam divergence) σ_θ in x and σ_ϕ in y
- beam emittance (beam size and divergence phase space area) $\epsilon_{x,\theta}$ in x and $\epsilon_{y,\phi}$ in y.

The spatial and angular beam spread distributions are Gaussian and correlated. This correlation is described by the emittance parameter defined as the elliptic phase space area and is responsible for the rotation of the phase space, as presented in figures 2(b), (c) and (d). The pencil beam source proposed allows us to define non-symmetrical spot configurations.
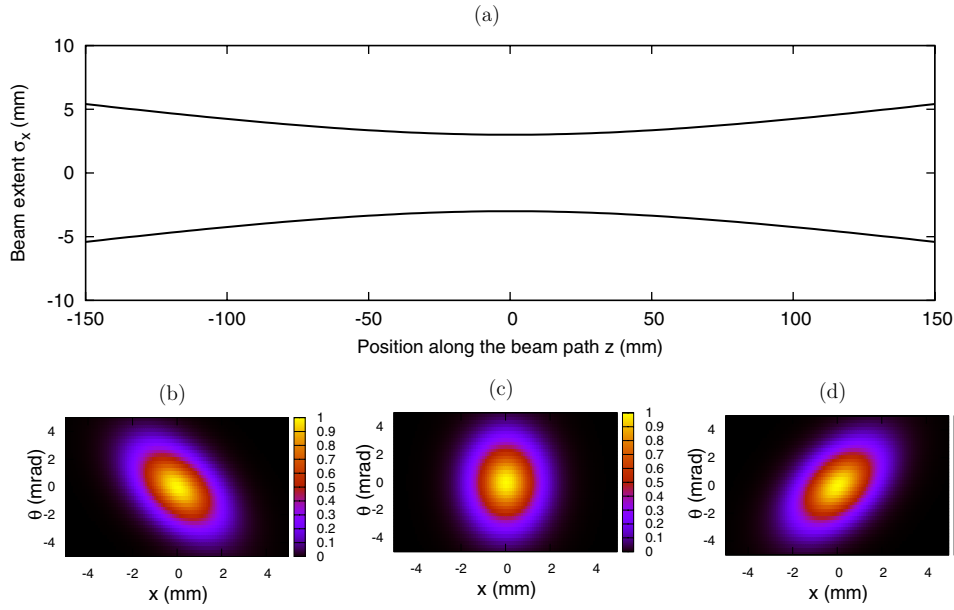
(a)

(b)   (c)   (d)

Figure 2. Illustration of the beam optical properties in the XoZ plan. (a) Beam size variations (σ_x) along the beam axis z, due to the beam divergence (σ_θ). The correlation between beam size (σ_x) and divergence (σ_θ) is illustrated in figures (b), (c) and (d), showing the rotation of the elliptic phase space along the beam axis at three positions, -120, 0 and $+120$ mm, respectively. The colored scale refers to the normalized proton probability density function in the phase space. A similar relationship holds in the YoZ plan.

2.1.2. GateSourceTPSPencilBeam. To simulate a treatment plan, the *GateSourceTPSPencil-Beam* source requires two input files: the *source description file* and the *plan description file*. The *source description file* describes the beam delivery system by a collection of polynomial equations allowing us to compute the optical and energy properties of every single pencil beam at the nozzle exit, as a function of the beam energy at the nozzle entrance. Therefore, it contains eight equations: two equations describe energy properties (E_0 and σ_E) and six describe optical properties (σ_x, σ_θ, $\epsilon_{x,\theta}$, σ_y, σ_ϕ, $\epsilon_{y,\phi}$), each equation being a function of the energy at the nozzle entrance. The user can define the polynomial order of each equation and then the corresponding coefficients. For instance, to define a N order polynomial equation for the energy spread $\sigma_E(E)$, the user must define the N coefficients a_i, with E the beam energy (at the nozzle entrance) and i the coefficient order:

$$\sigma_E(E) = \sum_{i=0}^{N} a_i \times E^i. \tag{1}$$

The *source description file* also contains the position of the two scanning magnets relatively to the isocenter and the distance between the nozzle exit and the isocenter, in order to compute the position and direction of each pencil beam at the nozzle exit. The *plan description file* describing the treatment plan contains one or multiple fields, each being described by a gantry angle and a collection of pencil beams (section 2.1.1).

 Each pencil beam is characterized by its weight, its position in the isocenter plan and its energy at the nozzle entrance. Weights can be expressed as a number of protons, or as monitor units (MU), that are internally converted into a number of protons as a function of
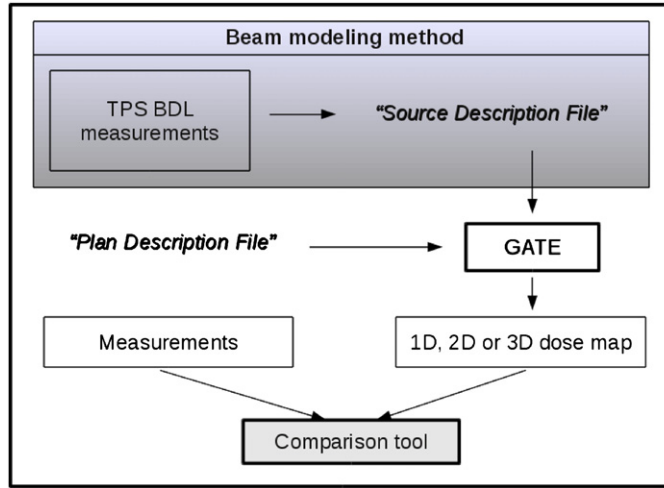
Figure 3. The proposed method allows for producing a *source description file* based on BDL measurements. This file together with a *plan description file* are then used as input in Gate for treatment plan simulation. The resulting simulated dose map is further compared with measurements using appropriate tools.

the proton stopping power in air. A treatment plan can be evaluated either by simulating all fields simultaneously or by simulating each field separately. The goal of the proposed method is to produce a specific *source description file* for each delivery system. The source description file produced in this paper is a property of IBA, but is available upon direct request to gate-modelrequest@iba-group.com. A schematic view of the global process allowing us to assess complex 3D treatment plans is presented in figure 3.

2.1.3. Modeling the beam optics. In this paper, 'spot size' will always refer to one standard deviation of the Gaussian spots. From spot size measurements at the nozzle exit and around the treatment isocenter (figure 4(a)), it was found that variations of the beam size with depth could be modeled linearly as a function of the distance to the isocenter for every energy (figure 4(b)).

The slope of the linear fit for each energy corresponds to the beam divergence and allows easy computation of the spot size at the nozzle exit. We further corrected the beam intrinsic divergence at the nozzle exit by eliminating any additional divergence due to scattering in air using a quadratic rule:

$$\sigma_{\theta_{Noz}}^2 = \sigma_{\theta_{Iso}}^2 - \sigma_{\theta_{Air}}^2, \tag{2}$$

where $\sigma_{\theta_{Noz}}$ is the intrinsic beam divergence in the x direction at the nozzle exit, $\sigma_{\theta_{Iso}}$ is the beam divergence in the x direction estimated from the measurements in air at the isocenter and $\sigma_{\theta_{Air}}$ is the estimated divergence increase due to interactions in air between the nozzle exit and the isocenter. The same rule was applied in the y direction. The divergence increase in air was estimated by Monte Carlo simulation and fitted using a second-order polynomial as a function of the beam energy. As the beam at the nozzle exit was considered purely divergent, the beam emittance was set empirically to half the beam size (at the nozzle exit) times the beam divergence times π. The beam size (σ_x and σ_y), divergence (σ_θ and σ_ϕ) and emittance ($\epsilon_{x,\theta}$ and $\epsilon_{y,\phi}$) estimated at the nozzle exit for 27 energies were then fitted using six polynomial
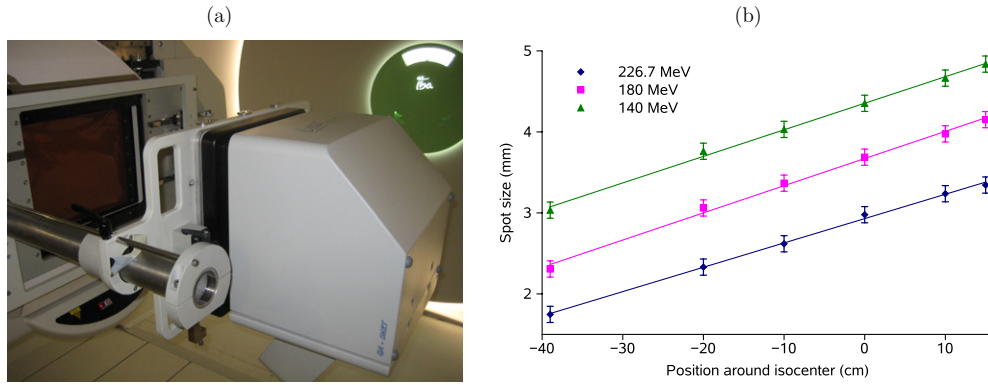
(a) (b)

Figure 4. (a) Illustration of the measurement of the dose profiles around the treatment isocenter: one can see the nozzle exit on the left and the sliding scintillating screen mounted on lateral rods on the right part. (b) Sample of the measured spot sizes for three energies and six positions. The points represent the measured values with associated error bars and the lines correspond to the linear modeling.
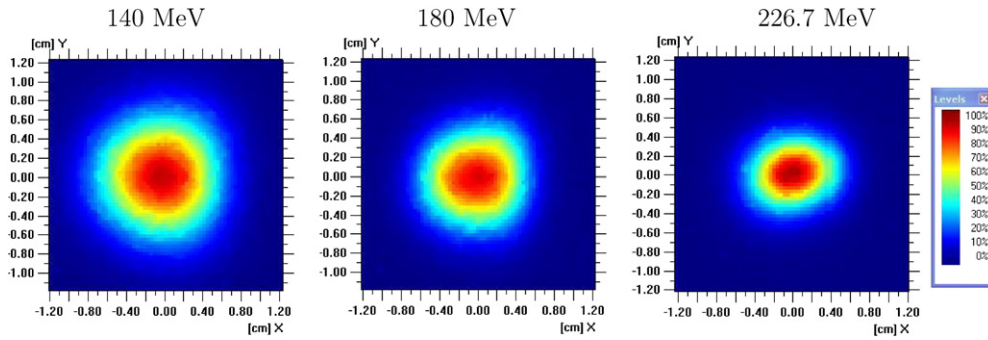

Figure 5. Sample of measured spots at the isocenter at three energies: 140, 180 and 226.7 MeV. The color scale represents the dose.

equations as a function of the energy at the nozzle entrance. The six equations obtained for the beam optical properties were inserted in the *source description file*. A sample of measured spots is presented in figure 5.

2.1.4. Modeling the energy spectrum. For each measured Bragg peak, we calculated the physical range in water, defined as the distal 80% dose point. A water equivalent path length was added to account for the energy loss in air between the nozzle exit and the patient. Conversion of ranges into energies was performed using the NIST PASTAR database (Berger *et al* 2009), as already presented in (Grevillot *et al* 2010). Finally, a third-order polynomial was used to fit the energy at the nozzle exit as a function of the energy at the nozzle entrance. The energy spread is a key parameter that influences the peak-to-plateau ratio and distal fall-off slope. We knew that its value increases from about 0% at 230 MeV, up to about 0.7% at 100 MeV (Grevillot *et al* 2010). As the fraction of energy scored in the ionization chamber depends also on the optical properties of the beam, the beam optic parameters presented in the previous section were integrated in the simulations. The best energy spread was then selected
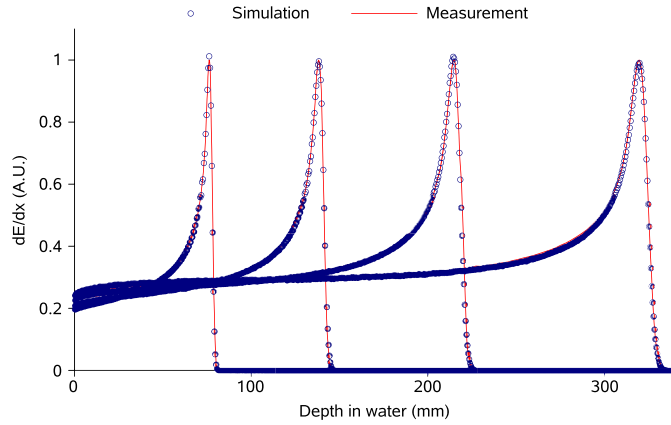
Figure 6. Sample of measured and simulated depth–dose profiles for four energies: 226.7, 180, 140 and 100 MeV.

empirically by simulating different energy distributions around the estimated value with 0.1 MeV resolution. The best energy spread was determined by evaluating the dose-to-peak and mean point-to-point dose differences. The dose-to-peak difference corresponds to the percentage of difference between measurement and simulation for the maximum dose point. The mean point-to-point deviation was evaluated using the following equation:

$$\epsilon = \sum_{i=1}^{N} \left(\frac{|d_i - dref_i|}{dref_i} \times \frac{\Delta_i}{L} \right), \tag{3}$$

where ϵ is the mean point-to-point dose deviation, i corresponds to a given curve point, N is the number of points evaluated, Δ_i is the distance between two consecutive points, L is the integration length and corresponds to the distance between the first measured point and the range, d_i and $dref_i$ are the evaluated and reference doses, respectively. Eventually, a third-order polynomial function was used to fit the curve of energy spread at the nozzle exit as a function of energy at the nozzle entrance. The two equations obtained for the beam physical properties were inserted in the *source description file*. A sample of measured and simulated depth–dose profiles is presented in figure 6.

The method presented to model the beam optics and energy spectrum of the system has to be performed once, and the *source description file* obtained can then be used as input for all subsequent treatment plan simulations.

2.2. Reference measurements

BDL measurements (depth–dose profiles and spots) were performed at 27 energies between 100 and 226.7 MeV, with a 5 MeV increment.

2.2.1. Spot sizes in air.

Spot sizes were measured in air at five depths around the isocenter: -20 cm, -10 cm, isocenter, $+10$ cm, $+15$ cm, in order to evaluate beam size variations with depth. Additional measurements were performed close to the nozzle exit (-39 cm), to better estimate the beam divergence (figure 4(b)). Measurements were performed using an electronic portal imaging device (Lynx, FIMEL) with a working area of 300×300 mm^2 and a pixel resolution of 0.5 mm. The device was attached to the nozzle using two lateral rods,

which allowed for sliding the scintillating screen at several predefined positions (figure 4(a)). The measurements were fitted automatically with a two-dimensional Gaussian function in order to accurately and reproducibly extract the spot sizes in the *x* and *y* directions. Spot size measurement accuracy was estimated to be within 0.1 mm.

2.2.2. Pristine Bragg peak in water. Pristine Bragg peaks were measured in a $60 \times 60 \times 60$ cm^3 water phantom (Blue Phantom®, IBA-Dosimetry). Two large Bragg peak chambers (PTW type 34070) with a 10.5 cm^3 sensitive volume and a collecting electrode of 81.6 mm in diameter were used, so that the proton beams were integrated within the sensitive volume of the chamber. The first chamber was placed at the phantom entrance and used as a reference chamber to eliminate beam fluctuations. The second chamber was placed in the phantom and moved along the beam axis with a step size between 0.3 mm in the Bragg peak region and 3 mm at high energy in the plateau region. The measured range accuracy was estimated to be within 0.5 mm and the measured dose fluctuations within 1%. It is noteworthy that pencil beams were not fully measured by the ionization chamber. It has been demonstrated using the MCNPX Monte Carlo code that scoring the energy in cylindrical tallies of radius 4.08 or 10 cm under-estimates the energy deposited in certain regions of the Bragg curve by up to 7.8% and 1.4%, respectively, when compared to energy scored in cuboid tallies with a resolution of $40 \times 40 \times 0.1$ cm^3 (Sawakuchi *et al* 2010). Cylindrical tallies with 4.08 cm radius represent the largest commercially available chambers. We performed similar comparisons using Geant4 for the highest system energy configuration, which delivers a 226.7 MeV beam, with a spot size of about 3 mm in air at the isocenter. The maximum dose differences observed were 5% and 1%, respectively, when comparing cylindrical dosels[3] of radius 4.08 cm and 10 cm, with square dosels of $40 \times 40 \times 0.1$ cm^3 (figure 7). Assuming that the maximum spot size of a 226.7 MeV proton beam in water is about 2.5 times that of the spot at the phantom entrance, the maximum spot size in this case is approximately 7.5 mm. We can consider that about 99.7% of the protons are located within three standard deviations, i.e. within 22.5 mm from the beam axis, while the chamber radius is 40.8 mm. Therefore, the missing energy is not likely to be associated to primary protons scattered outside the chamber volume by Coulomb scattering, but rather to non-elastic hadronic collisions and light fragments not measured by the chamber. This statement is supported by the results of a simulation showing that the maximum under-estimation of the deposited energy is somewhere around mid-range (figure 7).

As a consequence, the cylindrical geometry of the ionization chamber was always reproduced in the simulations in order to provide relevant comparisons with measurements.

2.3. Simulation environment

The number of processes, models and cross-section data available in Geant4 makes it not only flexible but also a complex tool to configure (Geant4-Collaboration 2009). There are also numerous parameters that can be adjusted, depending on the application type. For high precision simulations, Geant4 proposes a physics-list with default parameter values (Geant4 Electromagnetic Standard Working Group 2009). In previous works, we have investigated the main relevant parameters for proton therapy (Grevillot *et al* 2010) and carbon ion therapy (Zahra *et al* 2010) applications and their impact on the dose accuracy and computation time. Usually, the physics models and parameters used in Geant4 are referred to as 'physcis-list'. We decided to differentiate these two concepts by proposing a reference 'physics-list' with an optimized 'parameters-list', allowing us to reach a clinical level of dose accuracy with
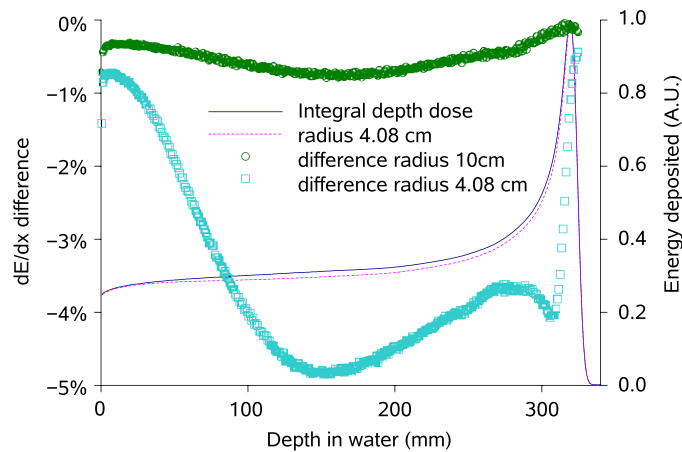
---

[3] dosel: dose scoring voxel.

Figure 7. Simulated dose difference between depth–dose profiles scored in cylindrical dosels of radius 4.08 and 10 cm, when compared to the depth–dose profiles scored in squared dosels of $40 \times 40 \times 0.1$ cm^3. Energy deposit difference corresponds to the left axis. The depth–dose profiles scored in squared dosels of $40 \times 40 \times 0.1$ cm^3 and in cylindrical dosels of 4.08 cm in radius are also presented and refer to the right axis.

high simulation efficiency. In this context, we used the Geant4 option three parameters with additional *stepLimiter*, *range cut* and *tracking cut* values of 1 mm (Grevillot *et al* 2010). We selected the standard electromagnetic package, combined with the precompound model for non-elastic hadronic interactions. The only difference from our previous work (Grevillot *et al* 2010) was the addition of a 1 mm *tracking cut*: as we did not produce secondaries with a range larger than 1 mm, we decided not to track them once their residual range was lower than 1 mm. Unless otherwise specified, the physics-list and parameters-list presented above were used by default. In order to assess simulations with reference measurements presented in section 2.2, depth–dose profiles were scored in cylindrical dosels of 4.08 cm in diameter with 0.5 mm resolution. Simulated and measured depth–dose profiles were normalized to the integral dose deposited. Simulation agreements with measurements were evaluated in terms of range, mean point-to-point and dose-to-peak differences. The clinical range refer to the distal 90% dose point in the Bragg peak and is used to define the treatment plans. Therefore, in this paper we evaluated the accuracy of the simulated clinical ranges, instead of the physical ranges. Spot sizes were scored using a *phase space actor* (Jan *et al* 2011), placed perpendicularly to the beam direction at different positions around the isocenter (according to the measurements), in order to score the proton fluence. A grid resolution of 0.5×0.5 mm^2 was used in order to reproduce the imaging device resolution. Gaussian fits were applied on the simulated spot profiles using ROOT (Brun and Rademakers 1997), in order to compare measured and simulated spot sizes. The simulation statistical uncertainties (as presented in Grevillot *et al* (2011)) were always below 2% and even below 1% in most of the cases.

3. Results and discussion

3.1. Assessment of single pencil beams

The proposed method allowed for estimating the optical and energy properties of the system at the nozzle exit, as a function of the energy at the nozzle entrance. Then, polynomial
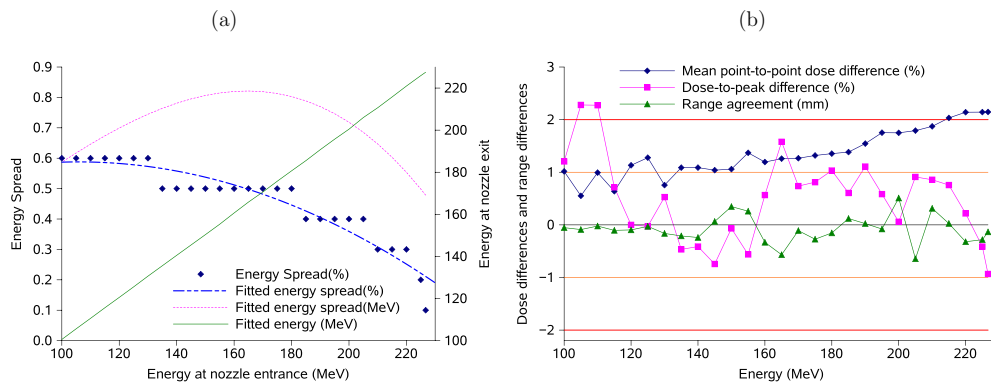
(a)   (b)

Figure 8. (a) Blue points correspond to the best energy spread estimation (in %), obtained with a 0.1% step. Based on these points, the relative (in %) and absolute (in MeV) energy spread at the nozzle exit were fitted as a function of the energy at the nozzle entrance and correspond to the dashed blue and dotted pink lines, respectively. The estimated energy at the nozzle exit is also presented as a green line and refers to the right axis. (b) Comparisons of simulated and measured Bragg peaks for 27 energies and the range agreement, mean point-to-point and dose-to-peak differences. Lines between the points are to guide the eyes only. Landmarks at ±2%, ±1% and 0% are also displayed.

equations were used to parametrize the estimated values. Therefore, for both optical and energy parameters, we first estimated the bias introduced by the parametrization. In a second stage, we assessed the global modeling accuracy by comparing simulated and measured values.

3.1.1. Depth–dose profiles. The maximum energy difference between the estimated and fitted energies was 0.27 MeV, resulting in a maximum range difference of 0.6 mm. In most of the cases however (>80% of the points), the range difference introduced by the fit was lower than 0.3 mm. The maximum energy spread difference introduced by the fit was 0.11 MeV. We recalculated the set of 27 Bragg peaks (using the *source description file*) and compared the clinical range agreement, the mean point-to-point and dose-to-peak differences. Results are presented in figures 8(a) and (b). For all energies tested, the clinical range agreement was better than 0.7 mm and even below 0.5 mm in most of the cases. Therefore, the main source of range discrepancy is not the Monte Carlo code itself, but rather the parametrization. The range precision of the model depends strongly on the range to energy calibration of the system: for instance, if the difference between the expected and the calibrated ranges of the system are alternatively +0.4, −0.4, +0.4 mm for three consecutive points, the fit function may introduce a range difference in the order of 0.5 mm for the mid point. The dose-to-peak and mean point-to-point dose differences were always below 2.3% and even below 2% in most of the cases. The mean point-to-point dose difference increased with energy, illustrating the better description of the Bragg peak at lower energy. The results obtained are clinically acceptable and validate the modeling of the energy parameters.

3.1.2. Spot sizes. The linear modeling of spot size variations with depth as presented in figure 4(b) allowed us to estimate the spot sizes within ±0.15 mm for 27 energies and for five positions around the isocenter and at the nozzle exit. The spot sizes around the isocenter were recalculated using the *source description file*. Results are presented in figure 9.
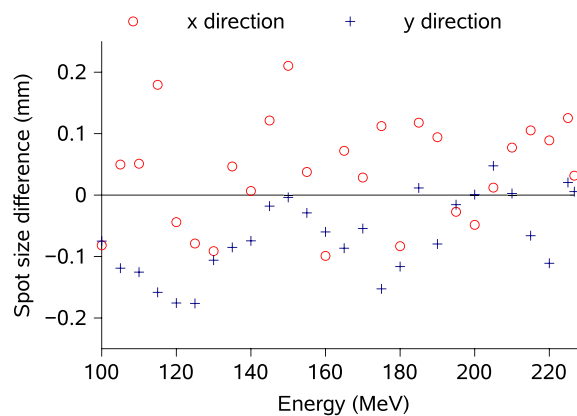
Figure 9. Difference between simulated and measured spot sizes at the isocenter for 27 energies in the *x* and *y* directions.

The measured spot sizes at the isocenter are reproduced by the simulation within ±0.2 mm. Therefore, as was the case for the energy spectrum, the main source of discrepancy is not the Monte Carlo code itself, but the parametrization. The modeling accuracy strongly depends on the smoothness of the spot size variations with energy. Sharp spot size variations around the trend-line are poorly accounted for by the model, as observed around 150 MeV in the *x* direction. Spot sizes were reproduced within ±0.4 mm for all other positions away from the isocenter. These results are clinically acceptable and validate the modeling of optical parameters.

3.2. Validation of the beam modeling using 2D and 3D plans

3.2.1. Spread-out Bragg peak. A spread out Bragg peak (SOBP) was measured in water using a PPC05 (IBA-Dosimetry) ionization chamber, with an active volume of 0.05 cm^3 and a collecting electrode of 1 cm in diameter. The chamber was placed in the water phantom and scanned along the beam axis with 10 and 2.5 mm steps in the plateau and SOBP regions, respectively. The treatment isocenter was set at 7 cm below the water surface. Measurements were based on a plan created using the XiO®TPS from Elekta. It contained one field made of 11 iso-energy layers modulated between 22 and 32 cm and 2446 spots with an iso-spacing of 8 mm in both directions, allowing the irradiation of a cube of 10 × 10 × 10 cm^3 in water. Simulated doses were scored in a cylindrical volume of 1 cm in diameter, with a 1 mm resolution, in order to simulate the cylindrical geometry of the chamber. The simulations were normalized to the measurements in the middle of the SOBP. They allowed us to evaluate the treatment plan integration in Gate, with respect to the accuracy of Geant4 models for dose calculation in water. Each single pencil beam had to be correctly modeled (*source description file*) and weighted (*plan description file*). The dose measured at each point depends not only on direct dose contributions from spots delivered along the beam axis and nearby pencil beams, but also on indirect dose contributions from nuclear interactions and secondary particles. The comparison between simulated and measured SOBPs is presented in figure 10. The result is satisfactory, with a clinical range agreement of 0.8 mm and a maximum dose difference below 2% for each point from the plateau region up to the distal fall-off. In the SOBP region, the measured ripples are nicely reproduced by the simulation. In the plateau region, the simulation
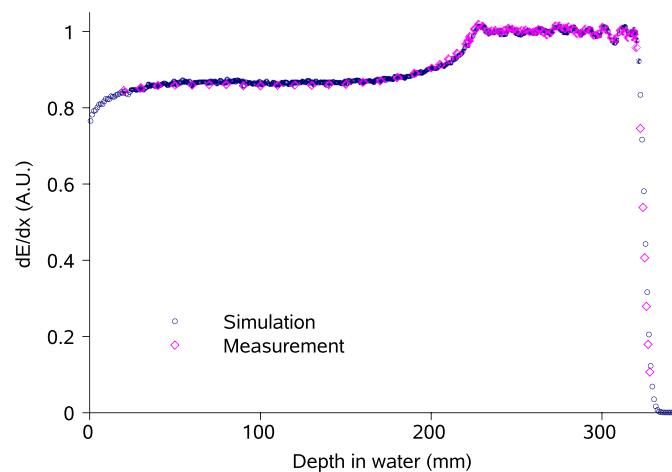
Figure 10. Comparison between simulation and measurement for a 32 cm range SOBP, modulated between 22 and 32 cm.

tends to overestimate the dose compared to measurements. The range and dose differences between simulation and measurements of the SOBP are consistent with the previous results obtained for pristine Bragg peaks.

3.2.2. Beam halo. The transverse dose spreading of each single pencil beam is due to Coulomb scattering interactions and hadronic collisions. The dose of a pencil beam can spread far away from its main axis, because of non-elastic nuclear interactions. This effect has been first referred to as *beam halo* (Pedroni *et al* 2005) and later as *low dose envelope* (Sawakuchi *et al* 2010). Beam spreading is mainly due to interactions in the propagating material, but it can also be inherent to the beam line, mainly due to scattering in some specific components (Sawakuchi *et al* 2010). The integral dose contribution due to nuclear interactions increases with depth, while the beam halo FWHM is maximum at about mid-range (Pedroni *et al* 2005). Nuclear collisions are more important with high energy beams and could be responsible for about 10–15% of the total dose (Pedroni *et al* 2005). The impact of the beam halo is difficult to measure for single pencil beams, while it is more visible with large fields. The field size factor (FSF) has been defined as the ratio between the dose at the center of a given square field with a given size f and the dose at the center of a square reference field with a size $f = 10$ cm (Sawakuchi *et al* 2010). We measured FSFs at several depths d (10, 20 and 30 cm), for four mono-energetic square fields (226, 200, 180 and 160 MeV) and for five field sizes (4, 6, 8, 10 and 12 cm). The spot spacing was 2.5 mm in the x and y directions and all spots had exactly the same weight. Measurements were performed with a Scanditronix Wellhofer CC13 ionization chamber having an active volume of 0.13 cm^3. Simulated doses were scored in $5 \times 5 \times 5$ mm^3 dosels, in order to reproduce the ionization chamber active volume. An increased dose in the center was expected for larger field sizes, as the number of pencil beams was higher. The additional dose measured for larger fields is assumed to result from either direct dose contribution from nearby pencil beams or indirect dose contribution from secondary protons and fragments resulting from nuclear interactions. We assumed that the direct dose contribution from a nearby pencil beam occurs only if the lateral distance between the beam and the center of the field is within three standard
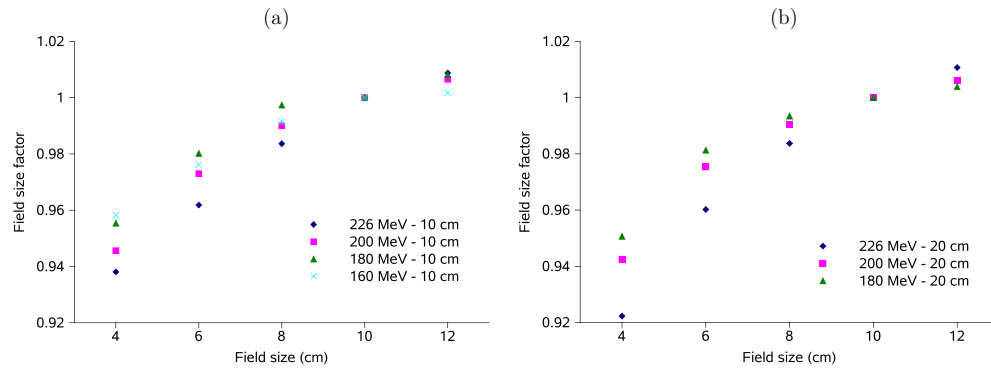
Figure 11. Measured FSFs: (a) for four energies and five field sizes at $d = 10$ cm, (b) for three energies and five field sizes at $d = 20$ cm.

Table 1. This table summarizes the FSF differences between simulations and measurements for four fields, three depths and four energies.

Energy (MeV)	226			200		180		160
f(cm) / d(cm)	10	20	30	10	20	10	20	10
4	1.4%	−0.4%	0.7%	1.0%	0.8%	0.4%	−0.3%	1.8%
6	2.4%	−0.8%	0.5%	0.3%	−0.8%	−0.5%	0.0%	2.0%
8	1.1%	−1.2%	−0.4%	0.0%	−0.6%	−1.3%	−1.9%	0.4%
12	0.1%	−3.2%	0.5%	−1.5%	−1.3%	−1.8%	−1.1%	−0.8%

deviations of the spot size. The largest spot size is about 8 mm in the Bragg peak region for a 226 MeV beam; hence, the largest lateral distance allowing direct dose contribution is about 2.4 cm. For other energies, direct dose contribution is restricted to $f = 4$ cm. Therefore, FSFs measured in these experiments are mainly representative of indirect dose contribution from non-elastic hadronic interactions. FSF simulations agreed with measurements within 2% for all but two points. The maximum difference was 3.2%. The overall results are satisfactory, even though there is no clear explanation for the larger 3.2% dose difference. As the number of non-elastic nuclear interactions increases with beam energy, larger differences between simulations and measurements are likely to occur at higher energies, notably due to uncertainties in nuclear cross sections. Uncertainties in total non-elastic and double-differential cross-sections are estimated in the order of 5–10% and 20–40%, respectively (ICRU 2000). Results are summarized in table 1. Due to nuclear interaction increase with energy, we expected larger FSF variations as a function of f at high energy compared to low energy. This was confirmed by measurements, as presented in figures 11(a) and (b). Interestingly, the opposite effect has been observed in a separate study (Sawakuchi *et al* 2010): larger FSF variations as a function of f were observed at low energy compared to high energy. In fact, the spot sizes were significantly bigger: about 4, 2 and 1.5 cm in FWHM, at 72.5, 148.8 and 221.8 MeV, respectively. Therefore, direct dose deposition from nearby pencil beams significantly contributed to the measured FSFs, even at low energy (largest spots), which might explain the inverse FSF variation trend associated with f. It is noteworthy that the range of energies in this study, from 72.5 MeV up to 221.8 MeV, was much larger than in our experiments, from 160 MeV up to 226 MeV.
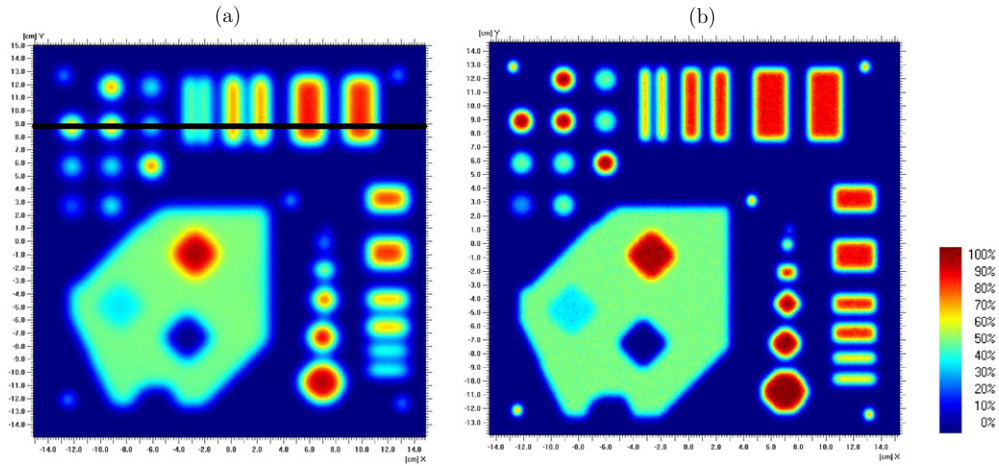
Figure 12. Measured dose map for the 117 MeV (a) and 226 MeV (b) beams. The extra black line drawn in (a) shows the position of the transverse dose profiles evaluated in figure 13. The low energy test pattern seems to be blurred, when compared to the high energy one, because the spot sizes are larger.

3.2.3. Test pattern. A two-dimensional test pattern consisting of a combination of particular shapes, in a field of 25×25 cm^2 was performed. This test, which contains a combination of homogeneous and high-gradient dose distributions was designed to evaluate the IBA's PBS system capabilities. Measurements were performed in air at the isocenter, using the Lynx scintillating device (described in section 2.2.1) at three energies: 117, 181 and 226 MeV, without insertion of additional material between the nozzle exit and the measuring tool. Figure 12 illustrates the measured dose maps for the 117 MeV and 226 MeV beams. For evaluating the system, the measured test patterns were compared to an expected dose map. Expected dose maps were calculated using the Matlab® software from MathWorks, by convolving the spot sizes and positions according to their weights. To evaluate our Monte Carlo code, the references were the measurements, but additional comparisons with the expected dose maps were also found to be useful. We will refer to these three types of dose map as measured, expected and simulated dose maps. This test allowed for evaluating the correct weighting and transverse position of each single pencil beam used in the treatment plan. In such a configuration, each proton contributes to one single point in the map. Therefore, the production time of each new proton becomes important when compared to its tracking time. Even the simulation time of the ionization process in air between the nozzle exit and the treatment isocenter becomes significant. Therefore, the range cut for secondary production due to electromagnetic interactions (electrons, positrons and photons) was set to 1 m. An additional volume of air of 5 cm thickness was set before the isocenter with a 1 mm range cut, in order to account for the electrons produced. This increased the simulation efficiency by a factor of 10. The dose maps were scored in water volume of $400 \times 400 \times 0.5$ mm^3 with a dosel size of $0.5 \times 0.5 \times 0.5$ mm^3, in order to mimic the scintillating device resolution. All dose maps (measured, expected and simulated) were normalized to 50% in a homogeneous region of interest located in the center of the test pattern, so that the maximum doses delivered were about 100%. Their origins were corrected using four landmarks located in each corner of the test pattern. We compared the two-dimensional dose-maps using the OmniPro-I'mRT® software (IBA-Dosimetry). Gamma indices were evaluated for all points receiving more than 0.2% of the maximum dose, using a 2%/2 mm criterion. At high energy, spot sizes are
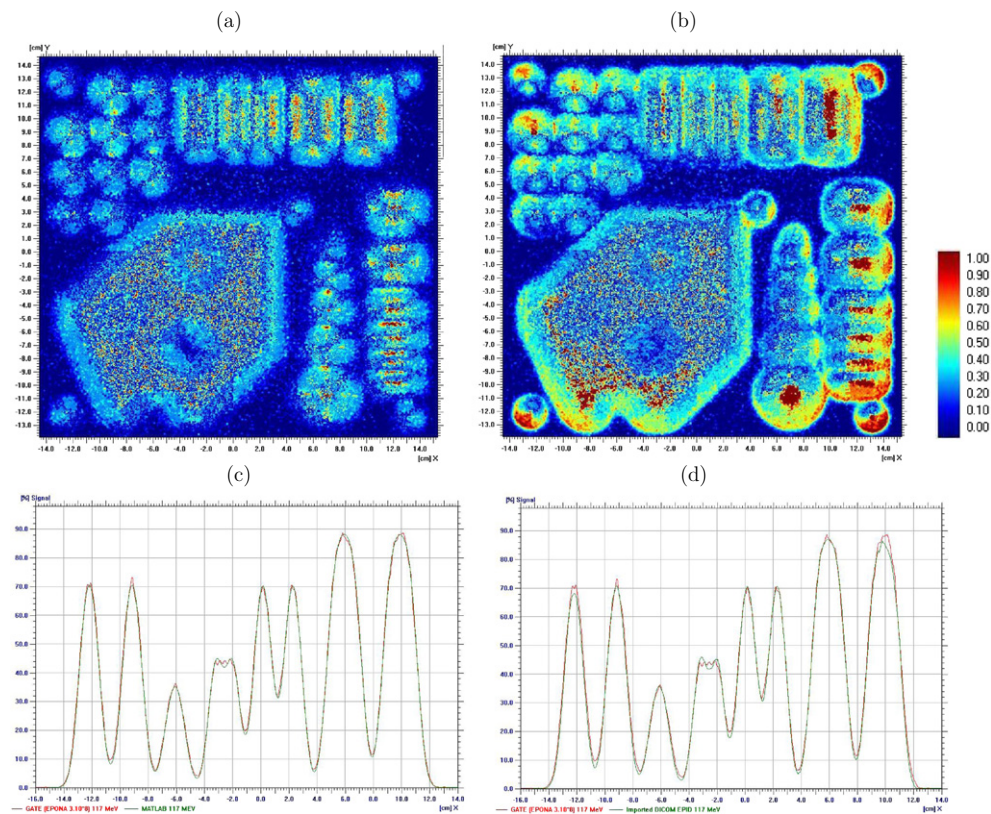
Figure 13. 2%/2 mm gamma index comparison between simulation and expected dose map (a) and between simulation and measurement (b), for the 117 MeV plan. Points having a gamma value larger than 1 do not pass the comparison. Transverse dose profile comparisons for the same beam energy, between simulation and expected dose map (c) and between simulation and measurement (d) are presented for the x direction at $y = 8.81$ cm, as referred to by the black line in figure 12(a).

known to be smaller and dose distributions sharper; hence, the gamma index comparisons were expected to be improved at low energy. Gamma index comparisons between simulations and measurements are summarized in table 2. The overall agreement between simulations and measurements is satisfactory, with a gamma index better than 97% for the three energies tested. Figure 13 shows transverse dose profiles and gamma comparisons between simulation and measurement and between simulation and expected dose map, for the 117 MeV plan. In high-dose regions, the maximal measured dose is lower than the simulated one. This could be due to a dose saturation effect in the detector. As all spots, but those in high-dose regions seem to be correctly weighted, we presume that the scintillating screen was saturated. When comparing simulations with expected dose maps, the dose overestimation in high-dose regions is no longer observed, consolidating the possibility of detector saturation. When comparing simulations with measurements, a larger disagreement is visible on the edge of the field. This disagreement is not visible when comparing simulations with expected dose maps, suggesting a dose measurement artifact on the side of the imaging device. Agreements are better between simulations and expected doses than between simulations and measurements. This is due to the fact that measurements and beam delivery suffer from other sources of uncertainty. As concerns measurements, dose saturation and side effects, such as dose response differences between the center and the sides of the imaging device may occur. As concerns the beam

Table 2. Gamma index comparisons for the 117, 181 and 226 MeV plans, using a 2%/2 mm gamma criterion.

Energy (MeV)	Gamma index
117	99.21%
181	98.98%
226	97.84%

delivery, beam positioning accuracy and reproducibility were not taken into account in the Monte Carlo code.

4. Conclusion

We have presented a generic method to model scanned ion beam delivery systems, without simulating the nozzle and based exclusively on BDL measurements of the system. New particle sources have been implemented in the Gate Monte Carlo platform in order to simulate single pencil beams and PBS treatment plans. The method has been applied to an IBA's proton PBS dedicated nozzle. The modeling of the irradiation system is based on a set of measurements at 27 energies between 100 and 226.7 MeV, containing depth–dose profiles in water and spot sizes in air. Simulated pristine Bragg peak ranges lie within 0.7 mm of measured values. Dose-to-peak and mean point-to-point differences between simulations and measurements are less than 2.3% for all energies. Spot sizes are reproduced within 0.4 mm around the isocenter (from −20 cm up to +15 cm) and within 0.2 mm at the isocenter. In a second stage, several 2D and 3D validation plans (SOBP, test pattern) were produced with the XiO treatment planing system. The simulation of a SOBP allowed for evaluating the correct intensity and physical properties of the delivered spots. The agreement was within 0.8 mm in range and 2% in dose for all points up to the distal fall-off. The simulation of FSF configurations for three depths, five field sizes and four energies, allowed us to evaluate the indirect dose contribution of secondary protons and fragments spreaded over the field. They laid within 2% for all points but two, with a maximum dose difference of 3.2%. A test pattern allowed for evaluating the correct position and intensity of each spot. More than 97% of the points successfully passed a 2%/2 mm gamma index comparison between simulations and measurements for three energies (117, 181 and 226 MeV). The validation tests performed so far have demonstrated that the beam model reaches clinical performances and can be used for TPS benchmarking. We believe that the proposed beam modeling method is sufficiently generic to be applied to other PBS systems with different types of ions, e.g. in active scanning carbon-therapy centers. The new tools presented are available in Gate release V6.1.

Acknowledgments

References

Amaldi U and Kraft G 2005 Radiotherapy with beams of carbon ions *Rep. Prog. Phys.* **68** 1861–82
Berger M J, Coursey J S, Zucker M A and Chang J 2009 *Stopping Powers and Ranges for Protons* National Institute of Standards and Technology (NIST) http://physics.nist.gov/PhysRefData/Star/Text/PSTAR.html

Brun R and Rademakers F 1997 ROOT—an object oriented data analysis framework *Proc. AIHENP '96 Workshop (Lausanne, Sept. 1996) Nucl. Instr. Meth.* A **389** 81–6

Chetty I J *et al* 2007 Report of the AAPM Task Group No. 105: issues associated with clinical implementation of Monte Carlo-based photon and electron external beam treatment planning *Med. Phys.* **34** 4818–53

Cirrone G A P, Cuttone G, Guatelli S, Nigro S L, Mascialino B, Pia M G, Raffaele L, Russo G and Sabini M G 2005 Implementation of a new Monte Carlo–GEANT4 simulation tool for the development of a proton therapy beam line and verification of the related dose distributions *IEEE* **52** 262–5

Geant4-Collaboration 2009 *Physics Reference Manual for Geant4* CERN http://www.geant4.org/geant4/support/index.shtml

Geant4 Electromagnetic Standard Working Group 2009 http://www.geant4.org

Grevillot L, Frisson T, Maneval D, Zahra N, Badel J N and Sarrut D 2011 Simulation of a 6 MV Elekta Precise Linac photon beam using GATE/GEANT4 *Phys. Med. Biol.* **56** 903

Grevillot L, Frisson T, Zahra N, Bertrand D, Stichelbaut F, Freud N and Sarrut D 2010 Optimization of GEANT4 settings for proton pencil beam scanning simulations using GATE *Nucl. Instrum. Methods Phys. Res. Sec. B: Beam Interact. Mater. At.* **268** 3295–305

ICRU 2000 Nuclear data for neutron and proton radiotherapy and for radiation protection *ICRU Report No 63* (Bethesda, MD: ICRU)

Jan S *et al* 2011 GATE V6: a major enhancement of the GATE simulation platform enabling modelling of CT and radiotherapy *Phys. Med. Biol.* **56** 881

Jan S *et al* 2004 GATE: a simulation toolkit for PET and SPECT *Phys. Med. Biol.* **49** 4543

Kawrakow I and Walters B R B 2006 Efficient photon beam dose calculations using DOSXYZnrc with BEAMnrc *Med. Phys.* **33** 3046–56

Lomax A J *et al* 2004 Treatment planning and verification of proton therapy using spot scanning: initial experiences *Med. Phys.* **31** 3150–7

Lomax A J, Bortfeld T, Goitein G, Debus J, Dykstra C, Tercier P A, Coucke P A and Mirimanoff R O 1999 A treatment planning inter-comparison of proton and intensity modulated photon radiotherapy *Radiother. Oncol.* **51** 257–71

Paganetti H, Jiang H, Lee S Y and Kooy H M 2004 Accurate Monte Carlo simulations for nozzle design and commissioning and quality assurance for a proton radiation therapy facility *Med. Phys.* **31** 2107–18

Paganetti H, Jiang H, Parodi K, Slopsema R and Engelsman M 2008 Clinical implementation of full Monte Carlo dose calculation in proton beam therapy *Phys. Med. Biol.* **53** 4825–53

Pedroni E, Scheib S, Böhringer T, Coray A, Grossmann M, Lin S and Lomax A 2005 Experimental characterization and physical modelling of the dose distribution of scanned proton pencil beams *Phys. Med. Biol.* **50** 541–61

Peterson S W, Polf J, Bues M, Ciangaru G, Archambault L, Beddar S and Smith A 2009 Experimental validation of a Monte Carlo proton therapy nozzle model incorporating magnetically steered protons *Phys. Med. Biol.* **54** 3217–29

Rogers D W O 2006 Fifty years of Monte Carlo simulations for medical physics *Phys. Med. Biol.* **51** R287–301

Sawakuchi G O, Mirkovic D, Perles L A, Sahoo N, Zhu X R, Ciangaru G, Suzuki K, Gillin M T, Mohan R and Titt U 2010 An MCNPX Monte Carlo model of a discrete spot scanning proton beam therapy nozzle *Med. Phys.* **37** 4960–70

Sawakuchi G O, Titt U, Mirkovic D, Ciangaru G, Zhu X R, Sahoo N, Gillin M T and Mohan R 2010 Monte Carlo investigation of the low-dose envelope from scanned proton pencil beams *Phys. Med. Biol.* **55** 711–21

Sawakuchi G O, Zhu X R, Poenisch F, Suzuki K, Ciangaru G, Titt U, Anand A, Mohan R, Gillin M T and Sahoo N 2010 Experimental characterization of the low-dose envelope of spot scanning proton beams *Phys. Med. Biol.* **55** 3467–78

Seco J, Jiang H, Herrup D, Kooy H and Paganetti H 2007 A Monte Carlo tool for combined photon and proton treatment planning verification *J. Phys.: Conf. Ser.* **74** 021014

Stankovskiy A, Kerhoas-Cavata S, Ferrand R, Nauraye C and Demarzi L 2009 Monte Carlo modelling of the treatment line of the Proton Therapy Center in Orsay *Phys. Med. Biol.* **54** 2377–94

Suit H *et al* 2010 Proton versus carbon ion beams in the definitive radiation treatment of cancer patients *Radiother. Oncol.* **95** 3–22

Tourovsky A, Lomax A J, Schneider U and Pedroni E 2005 Monte Carlo dose calculations for spot scanned proton therapy *Phys. Med. Biol.* **50** 971–81

Verhaegen F and Seuntjens J 2003 Monte Carlo modelling of external radiotherapy photon beams *Phys. Med. Biol.* **48** R107–64

Zahra N, Frisson T, Grevillot L, Lautesse P and Sarrut D 2010 Influence of Geant4 parameters on dose distribution and computation time for carbon ion therapy simulation *Physica. Medica.* **26** 202–8